

Aerodynamic Shape Optimization of Airfoils in Unsteady Flow

Anant Diwakar¹, D.N.Srinath¹ and Sanjay Mittal¹

Abstract: Aerodynamic shape optimization of airfoils is carried out for two values of Reynolds numbers: 10^3 and 10^4 , for an angle of attack of 5° . The objective functions used are (a) maximization of lift (b) minimization of drag and (c) minimization of drag to lift ratio. The surface of the airfoil is parametrized by a 4th order non-uniform rational B-Spline (NURBS) curve with 61 control points. Unlike the efforts in the past, the relatively large number of control points used in this study offer a rich design shape with the possibility of local bumps and valleys on the airfoil surface. The airfoils obtained via the optimization exhibit significantly improved aerodynamic performance compared to the NACA 0012 airfoil. Maximization of lift results in airfoils with corrugations on the upper surface. These corrugations are accentuated in the airfoils that are optimal at $Re = 10^4$. The improved performance is due to the formation of small vortices for the optimal airfoil. These vortices lead to an increase in suction on the airfoil surface. The time-averaged flow field shows that these vortices occupy the valleys in the corrugated upper surface of the optimal airfoil. Compared to a NACA 0012 airfoil, the time-averaged lift coefficient increases by 36.58% at $Re = 10^3$ and 220.72% at $Re = 10^4$, over the NACA 0012 airfoil. Minimization of drag results in airfoils with flatter upper surface. Compared to the NACA 0012 airfoil, the time-averaged drag coefficient for the optimal airfoil is 2.1% smaller at $Re = 10^3$. The reduction at $Re = 10^4$ is 15.36% compared to the NACA 0012 airfoil. The effect of the time period for time averaging of the flow, on the convergence of the optimization cycle, is investigated. It is found that time period for which the unsteady data is sampled and time-averaged should be sufficiently long time to achieve good convergence in the optimization cycle. A continuous adjoint based method is used for shape optimization. The flow as well as the adjoint equations are solved via a stabilized finite element method. The limited memory Broyden-Fletcher-Goldfarb-Shanno (L-BFGS) algorithm is used to minimize the objective function.

Keywords: shape optimization, adjoint methods, finite element, airfoil, unsteady

¹ Dept. of Aerospace Engineering, IIT Kanpur, 208016, India

flows

1 Introduction

There is a renewed interest in aerodynamics at low to moderate Reynolds numbers owing to its application in a variety of flows. Significant research has been carried out in the recent past to design airfoils for low Reynolds numbers flows. These airfoils are utilized in a variety of applications such as micro-aerial vehicles (MAV), unmanned aerial vehicles (UAV), small wind turbines and high altitude remotely piloted vehicles (RPV) [Mueller, Kellogg, Ifju, and Shkarayev (2006); Mueller and DeLaurier (2003); Lissaman (1983); Spedding and Lissaman (1998)].

Sunada [Sunada, Sakaguchi, and Kawachi (1997)] examined the aerodynamic characteristics of various airfoils at $Re = 4 \times 10^3$. They considered the variation of several parameters such as thickness, camber and roughness of the airfoils. The airfoils include several from the NACA four digit series with zero camber, flat plates with different thickness to chord ratios, thin plates with varied camber and a corrugated airfoil. They observed that at low Re , unlike at higher Re , thinner airfoils with a sharp leading edge exhibit better aerodynamic characteristics than their counterparts. The characteristics of airfoil are strongly affected by leading edge vortices.

The aerodynamics of insect flight has received significant attention in recent times. The insects operate at $Re \sim 10^4$ based on the wing parameters. Typically, the wings have pleated sections. Vargas and Mittal [Vargas, Mittal, and Dong (2008)] performed numerical study of flow past a modeled dragonfly wing section and compared the results with that of a corresponding profiled airfoil and flat plate at $Re = 10^4$. Numerical results show that the pleated airfoils exhibit a superior aerodynamic performance compared to the profiled airfoil and flat plate. Similar observations were also made by Okamoto [Okamoto and Azuma (2005)] via wind tunnel tests on dragonfly wing models.

Optimization is a useful tool for engineering design. A set of parameters are identified. These parameters are allowed to vary within the design space to maximize or minimize a pre-defined objective function. The process of optimization may be carried out to either realize an optimal topology or a shape [Bendsoe and Sigmund (2002)]. Topology optimization [Tapp, Hansel, Mittelstedt, and Becker (2004); Cisilino (2006); Wang, Lim, Khoo, and Wang (2007)] deals with the determination of optimal distribution of material within the design space of a structure. Some examples are the homogenization approach [Bendsoe and Kikuchi (1988)], variable density approach [Bendsoe and Sigmund (1999)], evolutionary structural optimization approach [Zhou and Rozvany (2001)] and optimality criteria method [Juan, Shuyao, Yuanbo, and Guangyao (2008)].

Several efforts to carry out aerodynamic shape optimization have been reported in the literature [Okumura and Kawahara (2000), Nadarajah and Jameson (2007)]. Various objective functions have been used. Some examples of the possible objective function are maximization of lift, minimization of drag and maximization of aerodynamic efficiency. Many methods for shape optimization have been proposed and successfully applied in the past. Adjoint based methods are of particular interest for problems with large number of design variables. In these methods the cost of computing the gradients of the objective functions is independent of the number of design variables. These methods are used widely in aerodynamic shape optimization [Jameson (1988), Anderson and Venkarakrishnan (1997)].

Srinath and Mittal [Srinath and Mittal (2007)] formulated a continuous adjoint based method for shape optimization and implemented it for steady low Reynolds number flows. The method was used for finding optimal airfoil shapes at low Re flows [Srinath and Mittal (2008)]. It was also utilized to carry out multi-point shape optimization of airfoils at low Re [Srinath, Mittal, and Manek (2009)]. In this effort an optimal airfoil is realized by carrying out optimization at several design points. The off-design performance of such airfoils are better compared to the designs obtained via single point optimization. The method proposed by Srinath and Mittal [Srinath and Mittal (2007)] was further extended for application to unsteady viscous flows [Srinath and Mittal (2010a)]. Optimal airfoil shapes were computed for the $Re = 10^4$ flow [Srinath and Mittal (2010b)]. In all these works, the airfoil geometry was parametrized via a 4th order NURBS curve with 13 control points. Although 13 control points are capable of representing fairly complex shapes, they are not enough to represent finer undulations on the surface of the airfoil. Higher number of control points are expected to provide a richer design space.

In the present work, an adjoint based optimization method is used to determine airfoil shapes with optimal aerodynamic performance at 5° angle of attack, at $Re = 10^3$ and 10^4 . The airfoil shape is parametrized by a 4th order NURBS curve with 61 control points. Interesting shapes are obtained for different objective functions. Some of these shapes are associated with undulations/corrugations which account for higher lift compared to optimal geometries obtained with lower number of control points.

2 Governing equations

2.1 Flow equations

Let $\Omega \subset R^{n_{sd}}$ and $(0, T)$ be the spatial and temporal domains, respectively, where n_{sd} is the number of space dimensions, and let Γ denote the boundary of Ω . The spatial and temporal co-ordinates are denoted by \mathbf{x} and t . The Navier-Stokes equations

governing incompressible flow are

$$\rho \left(\frac{\partial \mathbf{u}}{\partial t} + \mathbf{u} \cdot \nabla \mathbf{u} \right) - \nabla \cdot \boldsymbol{\sigma} = \mathbf{0} \quad \text{on } \Omega \times (0, T) \quad (1)$$

$$\nabla \cdot \mathbf{u} = 0 \quad \text{on } \Omega \times (0, T) \quad (2)$$

Here ρ , \mathbf{u} and $\boldsymbol{\sigma}$ are the density, velocity and stress tensor, respectively. The stress tensor is written as the sum of its isotropic and deviatoric parts:

$$\boldsymbol{\sigma} = -p\mathbf{I} + \mathbf{T}, \quad \mathbf{T} = 2\mu\boldsymbol{\varepsilon}(\mathbf{u}), \quad \boldsymbol{\varepsilon}(\mathbf{u}) = \frac{1}{2}(\nabla \mathbf{u} + (\nabla \mathbf{u})^T)$$

where p , \mathbf{I} and μ are the pressure, identity tensor and dynamic viscosity, respectively. The boundary conditions are either on the flow velocity or stress. Both, Dirichlet and Neumann type boundary conditions are accounted for:

$$\mathbf{u} = \mathbf{g} \quad \text{on } \Gamma_g \quad (3)$$

$$\mathbf{n} \cdot \boldsymbol{\sigma} = \mathbf{h} \quad \text{on } \Gamma_h \quad (4)$$

where, \mathbf{n} is the unit normal vector on the boundary Γ . Here, Γ_g and Γ_h are subsets of the boundary Γ . More details on the boundary conditions are given in Figure 1. Γ_U , Γ_D and Γ_S represent the upstream, downstream and lateral boundaries, respectively. The surface of the body is represented by Γ_B .

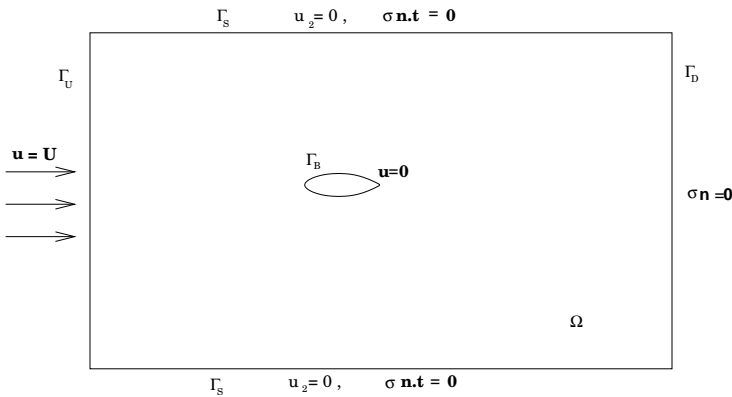


Figure 1: Schematic of the problem set-up: boundary conditions. Γ_U , Γ_D and Γ_S are the upstream, downstream and lateral boundaries, respectively and Γ_B is the body surface.

The initial condition on the velocity is specified on Ω :

$$\mathbf{u}(\mathbf{x}, 0) = \mathbf{u}_0 \quad \text{on } \Omega \quad (5)$$

where \mathbf{u}_0 is divergence free.

The drag and lift force coefficients, (C_d, C_l) , on the body are calculated using the following expression:

$$(C_d, C_l) = \frac{2}{\rho U^2 S} \int_{\Gamma_B} \boldsymbol{\sigma} \mathbf{n} d\Gamma \quad (6)$$

where, U is the free stream speed of the incoming flow and S is the characteristic area (plan area in present study).

The time-averaged coefficients are calculated as follows:

$$\overline{C_d} = \frac{1}{T} \int_{t_0}^{t_0+T} C_d(t) dt \quad (7)$$

$$\overline{C_l} = \frac{1}{T} \int_{t_0}^{t_0+T} C_l(t) dt \quad (8)$$

The time-averaging begins at $t = t_0$ to leave out the transient effect of the initial condition on the fully developed flow.

2.2 The continuous adjoint approach

Let Γ_B be the segment of the boundary whose shape is to be determined. Let $\boldsymbol{\beta} = (\beta_1, \dots, \beta_m)$ be the set of shape parameters that determine Γ_B . The optimization problem involves finding the shape parameters that minimize (or maximize) the objective function, $I_c(\mathbf{U}, \boldsymbol{\beta})$ subject to satisfying $\mathfrak{R}(\mathbf{U}, \boldsymbol{\beta}) = \mathbf{0}$, where \mathfrak{R} represents the flow equations. Depending on the accuracy needed various approximations to the flow equations could be used. The flow equations are treated as constraint conditions on the objective function. An augmented objective function is constructed to convert the constrained problem to an unconstrained one. The flow equations are augmented to the objective function by introducing a set of Lagrange multipliers or adjoint variables $\boldsymbol{\Psi}$.

$$I = I_c + \int_{\Omega} \boldsymbol{\Psi} \cdot \mathfrak{R} d\Omega \quad (9)$$

The augmented objective function (9) degenerates to the original one if the flow variables, \mathbf{U} , exactly satisfy the flow equations. The first variation of the augmented objective function is given by:

$$\delta I = \frac{\partial I}{\partial \mathbf{U}} \delta \mathbf{U} + \frac{\partial I}{\partial \boldsymbol{\beta}} \delta \boldsymbol{\beta} + \frac{\partial I}{\partial \boldsymbol{\Psi}} \delta \boldsymbol{\Psi} \quad (10)$$

The optimal solution is achieved when the variation of the augmented objective function vanishes, i.e., $\delta I = 0$. This requires that the variation of I with respect to the flow variables \mathbf{U} , design parameters $\boldsymbol{\beta}$ and the adjoint variables $\boldsymbol{\Psi}$ should go to zero, independently. These variations are given as:

$$\frac{\partial I}{\partial \boldsymbol{\Psi}} = \boldsymbol{\mathfrak{R}}(\mathbf{U}, \boldsymbol{\beta}) \quad (11)$$

$$\frac{\partial I}{\partial \mathbf{U}} = \left(\frac{\partial I_c}{\partial \mathbf{U}} + \int_{\Omega} \boldsymbol{\Psi}^T \frac{\partial \boldsymbol{\mathfrak{R}}}{\partial \mathbf{U}} d\Omega \right) \quad (12)$$

$$\frac{\partial I}{\partial \boldsymbol{\beta}} = \left(\frac{\partial I_c}{\partial \boldsymbol{\beta}} + \int_{\Omega} \boldsymbol{\Psi}^T \frac{\partial \boldsymbol{\mathfrak{R}}}{\partial \boldsymbol{\beta}} d\Omega \right) \quad (13)$$

Setting the variation of I with respect to $\boldsymbol{\Psi}$ to zero gives back the flow equations. The variation of I with respect to \mathbf{U} , given by Equation (12), when set to zero, leads to a set of equations and boundary conditions that are used to evaluate the adjoint variables. The gradient, $\frac{\partial I}{\partial \boldsymbol{\beta}}$, given by Equation (13) is utilized to find the optimal shape parameters. When the flow and adjoint equations are satisfied, the augmented objective function is seen to be a function only of the design parameters. This implies that the gradient can be determined without the need for additional flow computations, i.e. the cost of evaluating the gradients is independent of the number of design parameters.

2.3 Adjoint equations

The equations and boundary conditions for the adjoint variables are obtained by setting the variation of I with respect to the flow variables \mathbf{U} , given in equation (12), to zero. The equations governing the adjoint variables are:

$$\rho \left(-\frac{\partial \boldsymbol{\Psi}_u}{\partial t} + (\nabla \mathbf{u})^T \boldsymbol{\Psi}_u - (\mathbf{u} \cdot \nabla) \boldsymbol{\Psi}_u \right) - \nabla \cdot \boldsymbol{\sigma}_{\boldsymbol{\Psi}} = \mathbf{0} \text{ on } \Omega \times (0, T) \quad (14)$$

$$\nabla \cdot \boldsymbol{\Psi}_u = 0 \text{ on } \Omega \times (0, T) \quad (15)$$

where, $\boldsymbol{\sigma}_{\boldsymbol{\Psi}}$ is similar to the stress tensor and is given by $\boldsymbol{\sigma}_{\boldsymbol{\Psi}} = -\psi_p \mathbf{I} + \mu [\nabla \boldsymbol{\Psi}_u + (\nabla \boldsymbol{\Psi}_u)^T]$.

The adjoint equations (14) and (15) are a set of coupled linear partial differential equations. Unlike the flow equations (1) and (2), the equations for the adjoint variables are posed backward in time.

The boundary conditions on the adjoint variables are:

$$\boldsymbol{\Psi}_u = \mathbf{0} \text{ on } \Gamma_U \quad (16)$$

$$\mathbf{s} = \mathbf{0} \text{ on } \Gamma_D \tag{17}$$

$$s_1 = 0, \quad \psi_{u2} = 0 \text{ on } \Gamma_S \tag{18}$$

$$-\int_0^T \int_{\Gamma_B} \delta(\boldsymbol{\sigma} \cdot \mathbf{n}) \cdot \boldsymbol{\psi}_u d\Gamma dt + \frac{\partial I_c}{\partial \mathbf{u}} \delta \mathbf{u} + \frac{\partial I_c}{\partial p} \delta p = \mathbf{0} \text{ on } \Gamma_B \tag{19}$$

where, $\mathbf{s} = \{\mathbf{u}\boldsymbol{\psi}_u - \mathbf{I}\psi_p + \nu[\nabla\boldsymbol{\psi}_u + (\nabla\boldsymbol{\psi}_u)^T]\} \cdot \mathbf{n}$. Γ_U , Γ_D and Γ_S represent the upstream, downstream and lateral boundaries, respectively. The surface of the body is represented by Γ_B . The terminal condition on the adjoint velocity is given by:

$$\boldsymbol{\psi}_u(\mathbf{u}, T) = \mathbf{0} \text{ on } \Omega \tag{20}$$

The conditions on the boundary, given by equation (19), depend on the definition of the objective function.

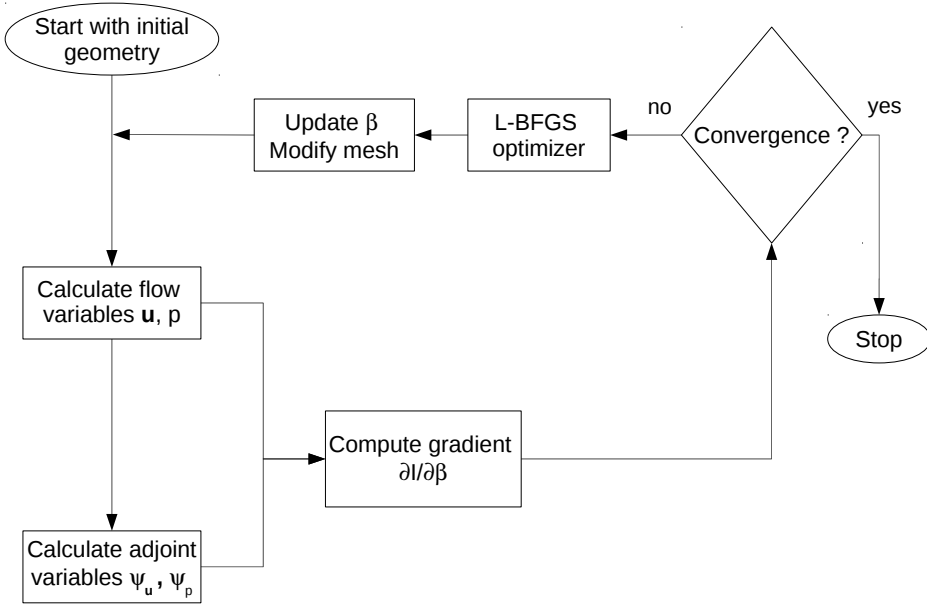


Figure 2: A flow-chart detailing the steps of the optimization process.

In the present work, the adjoint variables are computed once the time integration of the flow equations has been carried out and results stored. The flow and the adjoint

equations are solved by a stabilized finite element method based on streamline-upwind Petrov/Galerkin (SUPG) and pressure stabilized Petrov/Galerkin (PSPG), as discussed in [Srinath and Mittal (2010a)]. The limited memory Broyden-Fletcher-Goldfarb-Shanno (L-BFGS) algorithm is used to minimize the objective function [Byrd, Lu, Nocedal, and Zhu (1995)]. A conceptual algorithm for the iterative approach is shown in Figure 2.

In the present work, the optimization process is stopped if either the change in objective function, compared to the value in the previous iteration or the L_2 norm of the gradient is less than 10^{-5} .

3 Results

Shape optimization is carried out to design an airfoil which exhibits good aerodynamic performance. The computations are done for two values of Reynolds numbers: 10^3 and 10^4 . The design is carried out for an angle of attack of 5° . The surface of the airfoil is parametrized via Non-Uniform Rational B-Splines (NURBS). A curve represented via NURBS is defined as:

$$\mathbf{C}(t) = \frac{\sum_{i=0}^n N_{i,p}(t) w_i \mathbf{P}_i}{\sum_{i=0}^n N_{i,p}(t) w_i} \quad (21)$$

Here, n is the number of control points, p is the order of the curve, t is the knot vector, w_i is the weight associated with control point \mathbf{P}_i and $N_{i,p}$ are the B-Spline basis functions given by:

$$N_{i,0} = \begin{cases} 1 & \text{if } t_i \leq t \leq t_{i+1} \\ 0 & \text{otherwise} \end{cases} \quad (22)$$

$$N_{i,p} = \frac{t - t_i}{t_{i+p} - t_i} N_{i,p-1}(t) + \frac{t_{i+p+1} - t}{t_{i+p+1} - t_{i+1}} N_{i+1,p-1}(t) \quad (23)$$

In the present work the airfoil is parametrized by a 4^{th} order NURBS curve with 61 control points.

The airfoil is parameterized by a 4^{th} order NURBS curve with 61 control points. These control points form the design space for the optimization problem. The y coordinate of the control points is taken as the design variable. The airfoil shape is changed by changing the y coordinate of the control points. The control points at the leading and trailing edge are kept fixed whereas the remaining are allowed to move between specified upper and lower bounds, the maximum limit being 10% of the thickness of NACA 0012 airfoil. Three objective functions are chosen: (a) maximization of \overline{C}_l , (b) minimization of \overline{C}_d and (c) minimization of $\overline{C}_d/\overline{C}_l$. The mesh

consists of 51868 nodes and 103382 triangular elements with 250 nodes on the airfoil surface. A structured mesh is employed near the airfoil surface and in the near wake to resolve the flow structures adequately. The remaining domain is filled with unstructured mesh obtained via Delaunay triangulation. A mesh moving scheme is utilized to relocate the nodes of the mesh to accommodate the modified airfoil geometry. In this work, the shape optimization is conducted for an airfoil which is parametrized by a 4th order NURBS curve with 61 control points. Srinath and Mittal [Srinath and Mittal (2008)] studied the effect of varying the number of control points on the optimization process. It was observed that with more design variables, the design space becomes richer and the optimizer is able to determine a better solution, but at the cost of increased computation. Three different parametrizations having 13, 19 and 27 control points were used to define the NURBS curve during the optimization cycle.

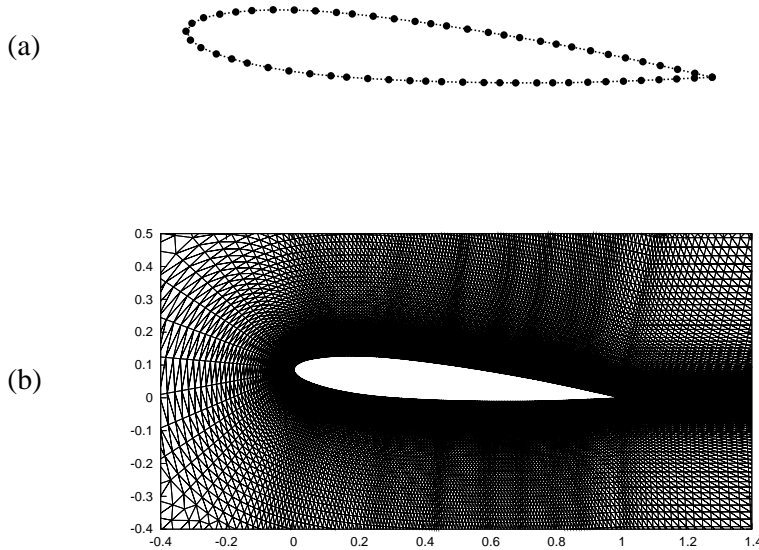


Figure 3: (a) Representation of NACA 0012 airfoil with NURBS curve with 61 control points (b) finite element mesh for NACA 0012 airfoil at 5° angle of attack.

3.1 Maximizing the time-averaged lift coefficient

The objective is to find the optimal shape airfoil with largest time-averaged lift coefficient. The objective function is defined as:

$$I_c = -\frac{1}{2}\overline{C_l}^2 \quad (24)$$

The optimization algorithm used in the present work minimizes the objective function. Hence a negative sign is used for the case of maximization of lift.

The computations begin with a geometry corresponding to a NACA 0012 airfoil. The optimal shape obtained for $Re = 10^3$ is shown along with the initial shape in Figure 4. The iteration history of $\overline{C_l}$ and the time history of C_l for the initial and final shapes are shown in Figure 5. The flow is very close to being steady. The time-averaged lift coefficient increases from 0.246 to 0.336. This corresponds to an increase of 36.58% over the NACA 0012 airfoil. The time-averaged streamlines and $\overline{C_p}$ distribution for the NACA 0012 and the optimal shape are shown in the Figure 6. From the figure, it is observed that a small bubble is formed on the upper surface near the leading edge, which results in increase in suction pressure and hence the increase in lift. The optimal shape appears to have evolved from the NACA 0012 airfoil to support this bubble. The pressure distribution for the NACA 0012 and the optimal shape are shown in Figure 7. The instantaneous vorticity field for the NACA 0012 and optimal shape at $t = 25$ are shown in Figure 8.

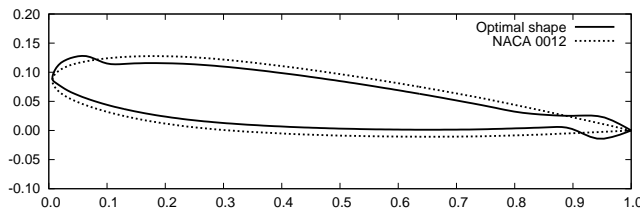


Figure 4: Initial and optimal shapes for maximization of $\overline{C_l}$ at $Re = 10^3$ and $\alpha = 5^\circ$.

The optimal shape obtained for $Re = 10^4$ is shown along with the initial shape in Figure 9. The iteration history of $\overline{C_l}$ and the time history of C_l for the initial and final shapes are shown in Figure 10. The time-averaged lift coefficient increases from 0.222 to 0.712; an increase of 220.72% over the NACA 0012 airfoil. The optimal shape obtained has corrugations on the upper surface. The time-averaged streamlines and $\overline{C_p}$ distribution for the NACA 0012 and the optimal shape are shown in

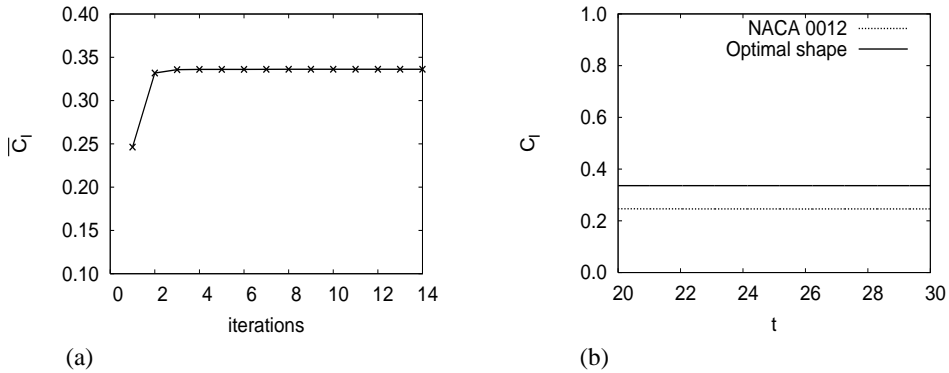


Figure 5: Maximization of $\overline{C_l}$ at $Re = 10^3$ and $\alpha = 5^\circ$:(a) iteration history of $\overline{C_l}$ (b) time history of C_l for initial and optimal shapes.

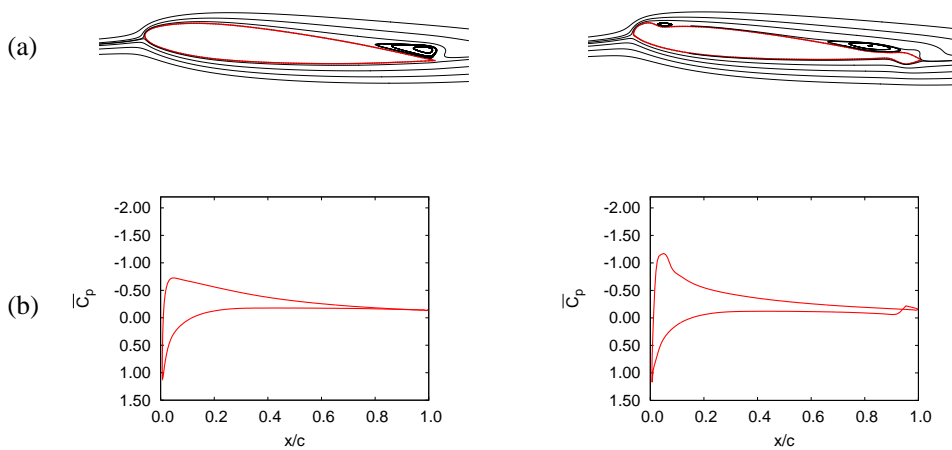


Figure 6: Maximization of $\overline{C_l}$ at $Re = 10^3$ and $\alpha = 5^\circ$:(a) time-averaged streamlines for NACA 0012 and optimal shape (b) $\overline{C_p}$ distribution for NACA 0012 and optimal shape.

Figure 11. From the streamline plot, it is observed that the time-averaged flow is associated with small vortices which sit in the valleys of the corrugations. These vortices lead to increase in the suction and hence, the lift. The time-averaged pressure distribution for the initial and optimal shapes are shown in Figure 12. It confirms

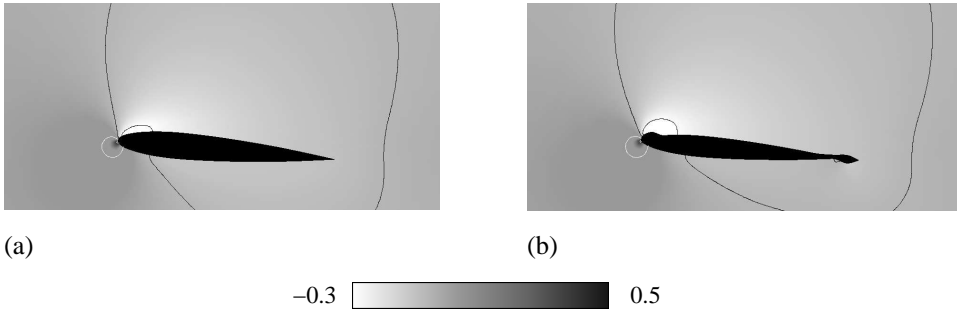


Figure 7: Maximization of $\overline{C_l}$ at $Re = 10^3$ and $\alpha = 5^\circ$: time-averaged pressure distribution for (a) NACA 0012 (b) optimal shape.

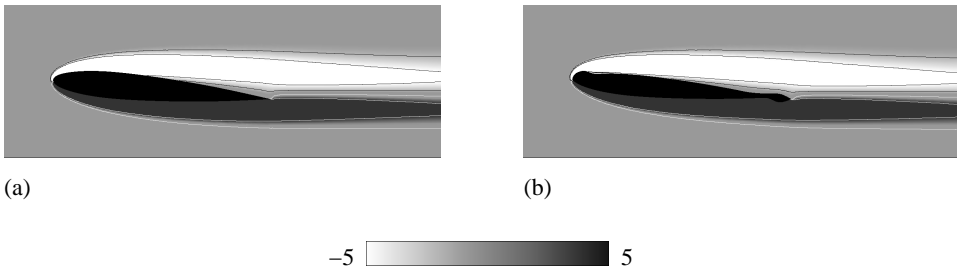


Figure 8: Maximization of $\overline{C_l}$ at $Re = 10^3$ and $\alpha = 5^\circ$: instantaneous vorticity field at $t = 25$ for (a) NACA 0012 (b) optimal shape.

the observation from the $\overline{C_p}$ distribution that the suction on the upper surface of the optimal airfoil is for a far more significant extent compared to that for a NACA 0012 airfoil. The instantaneous vorticity fields for the NACA 0012 and optimal shape at various time instants are shown in Figure 13. The separated shear layer for the NACA 0012 airfoil rolls up into vortices towards the trailing edge of the airfoil. In contrast, the shear layer for the optimal airfoil appears to lose stability close to the mid-chord of the airfoil as indicated by the undulations in the separated shear layer and presence of shear layer vortices.

3.2 Minimizing the time-averaged drag coefficient

The objective is to find the optimal shape airfoil with least time-averaged drag coefficient. The objective function is defined as:

$$I_c = \frac{1}{2} \overline{C_d}^2 \quad (25)$$

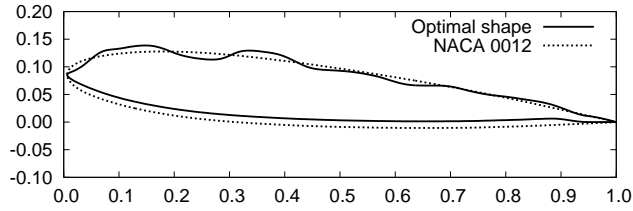


Figure 9: Initial and optimal shapes for maximization of \overline{C}_l at $Re = 10^4$ and $\alpha = 5^\circ$.

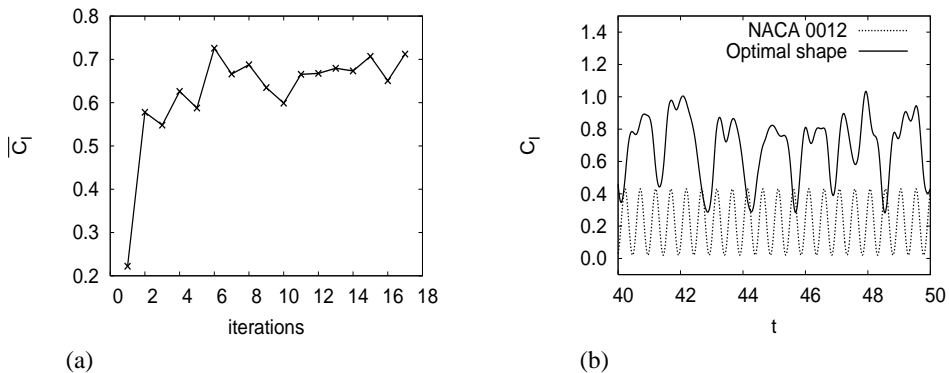


Figure 10: Maximization of \overline{C}_l at $Re = 10^4$ and $\alpha = 5^\circ$: (a) iteration history of \overline{C}_l (b) time history of C_l for initial and optimal shapes.

The computations begin with a geometry corresponding to a NACA 0012 airfoil. The optimal shape obtained for $Re = 10^3$ is shown along with the initial shape in Figure 14. The iteration history of \overline{C}_d and the time history of C_d are shown in Figure 15. The time-averaged drag coefficient decreases from 0.1264 to 0.1238; a decrease of 2.1% over the NACA 0012 airfoil. The time-averaged streamlines for the NACA 0012 and the optimal shape are shown in Figure 16. From the streamline plot, it is observed that the flow separation is delayed for the optimal shape as compared to NACA 0012. The pressure and the viscous components of the drag for the initial and optimal shapes are shown in Figure 17. From this figure, we conclude that the reduction in the drag of the optimal airfoil is mainly a result of the decrease in skin friction. The instantaneous vorticity field for the NACA 0012 and optimal shape at $t = 25$ are shown in Figure 18.

The optimal shape obtained for $Re = 10^4$ is shown along with the initial shape in

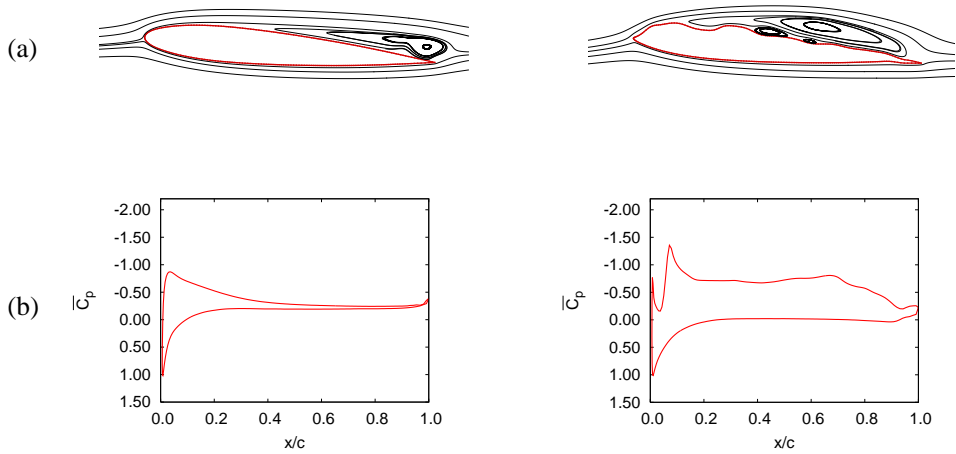


Figure 11: Maximization of $\overline{C_l}$ at $Re = 10^4$ and $\alpha = 5^\circ$:(a) time-averaged streamlines for NACA 0012 and optimal shape (b) $\overline{C_p}$ distribution for NACA 0012 and optimal shape.

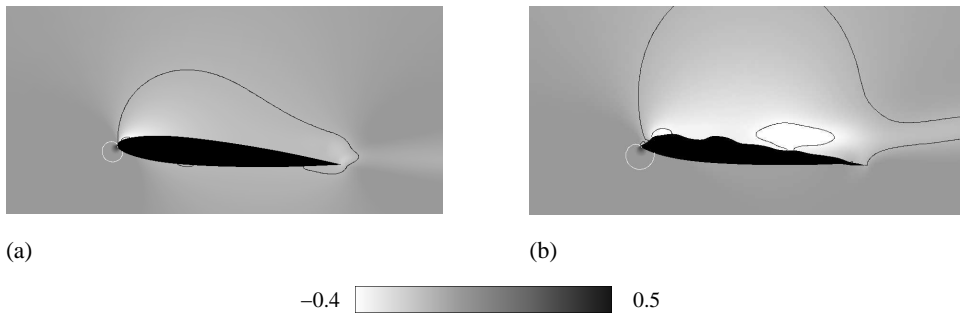


Figure 12: Maximization of $\overline{C_l}$ at $Re = 10^4$ and $\alpha = 5^\circ$: time-averaged pressure distribution for (a) NACA 0012 (b) optimal shape.

Figure 19. The iteration history of $\overline{C_d}$ and the time history of C_d are shown in Figure 20. For $Re = 10^4$, the time-averaged drag coefficient decreases from 0.0599 to 0.0507; a decrease of 15.36% over the NACA 0012 airfoil. The optimal shape obtained has a flatter profile on the upper surface. The time-averaged streamlines for the NACA 0012 and the optimal shape are shown in Figure 21. From the streamline plot, it is observed that the flow separation is suppressed near the trailing edge. The pressure and viscous drag for the initial and the optimal shapes are shown is

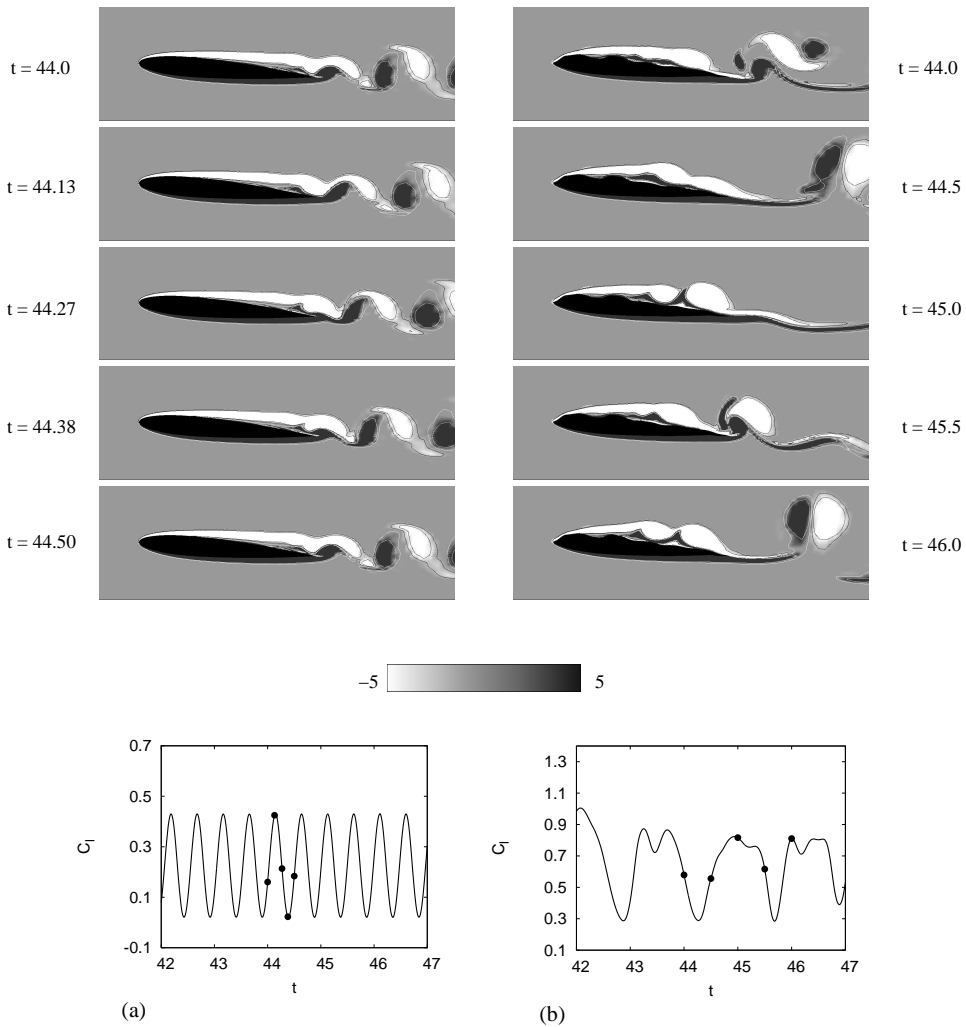


Figure 13: Maximization of $\overline{C_l}$ at $Re = 10^4$ and $\alpha = 5^\circ$: instantaneous vorticity fields at various time instants for (a) NACA 0012 (b) optimal shape.

Figure 22. As is seen for $Re = 10^3$, the decrease in drag for the optimal airfoil is mainly via the reduction in the skin friction. The instantaneous vorticity field for the NACA 0012 and optimal shape at $t = 44.5$ are shown in Figure 23. Compared to the NACA 0012 airfoil, the separated shear layer of the optimal airfoil rolls up into small vortices at a more upstream location leading to a reattachment of the flow, as observed in the time-averaged streamlines in Figure 21.

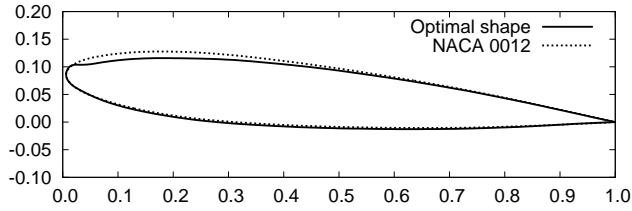


Figure 14: Initial and optimal shapes for minimization of $\overline{C_d}$ at $Re = 10^3$ and $\alpha = 5^\circ$.

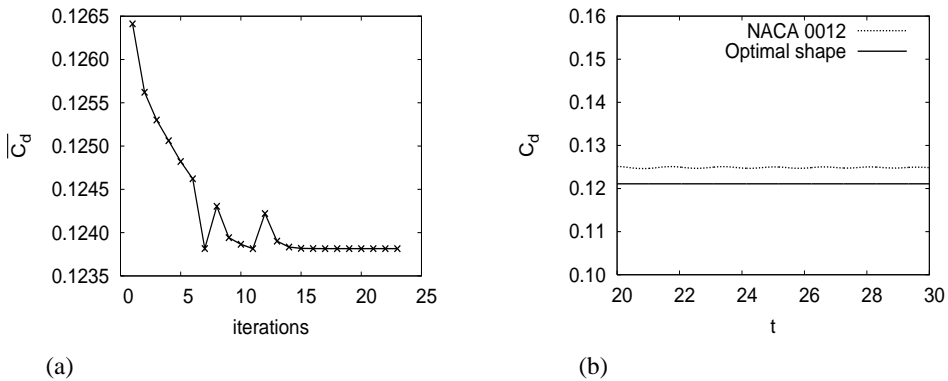


Figure 15: Minimization of $\overline{C_d}$ at $Re = 10^3$ and $\alpha = 5^\circ$: (a) iteration history of $\overline{C_d}$ (b) time history of C_d for initial and optimal shapes.



Figure 16: Minimization of $\overline{C_d}$ at $Re = 10^3$ and $\alpha = 5^\circ$: time-averaged streamlines for (a) NACA 0012 (b) optimal shape.

3.3 Maximizing aerodynamic efficiency

The objective is to find the optimal shape airfoil having maximum aerodynamic efficiency. The initial airfoil is NACA 0012 at 5° angle of attack. The objective is

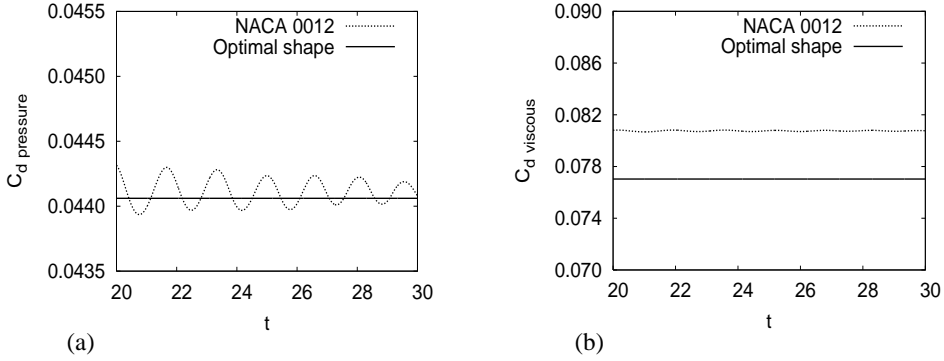


Figure 17: Minimization of $\overline{C_d}$ at $Re = 10^3$ and $\alpha = 5^\circ$: time history of (a) pressure drag for NACA 0012 and optimal shape (b) viscous drag for NACA 0012 and optimal shape.

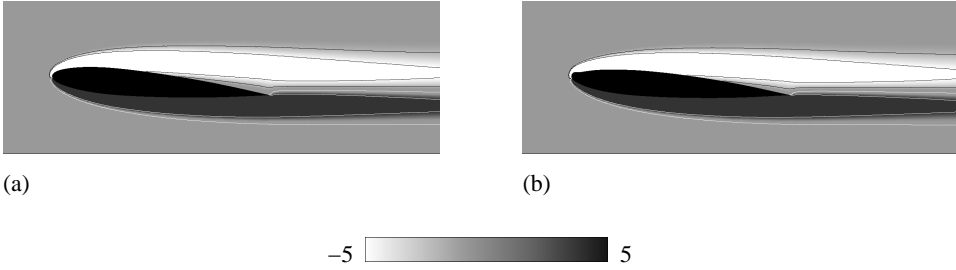


Figure 18: Minimization of $\overline{C_d}$ at $Re = 10^3$ and $\alpha = 5^\circ$: instantaneous vorticity field at $t = 25$ for (a) NACA 0012 (b) optimal shape.

to maximize $\overline{C_l}/\overline{C_d}$ which is equivalent to minimizing $\overline{C_d}/\overline{C_l}$. The objective function is defined as:

$$I_c = \frac{1}{2} \left(\frac{\overline{C_d}}{\overline{C_l}} \right)^2 \quad (26)$$

The optimal shape for $Re = 10^3$ is shown along with the initial shape in Figure 24. The iteration history of $\overline{C_d}/\overline{C_l}$ is shown in Figure 25. The time-averaged drag to lift ratio decreases from 0.513 to 0.382; a decrease of 25.53% over the NACA 0012 airfoil. The iteration histories of time-averaged lift and drag coefficient are shown in Figure 25. It is observed that the $\overline{C_l}$ increases from 0.246 to 0.318; an increase of 29.27%, whereas $\overline{C_d}$ decreases from 0.126 to 0.121; a decrease of 3.97%. Hence

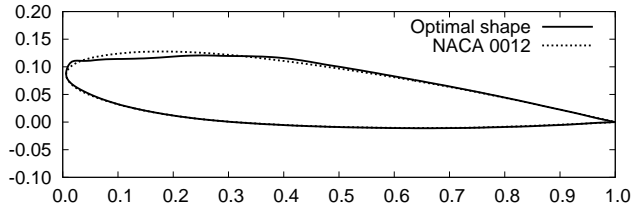


Figure 19: Initial and optimal shapes for minimization of $\overline{C_d}$ at $Re = 10^4$ and $\alpha = 5^\circ$.

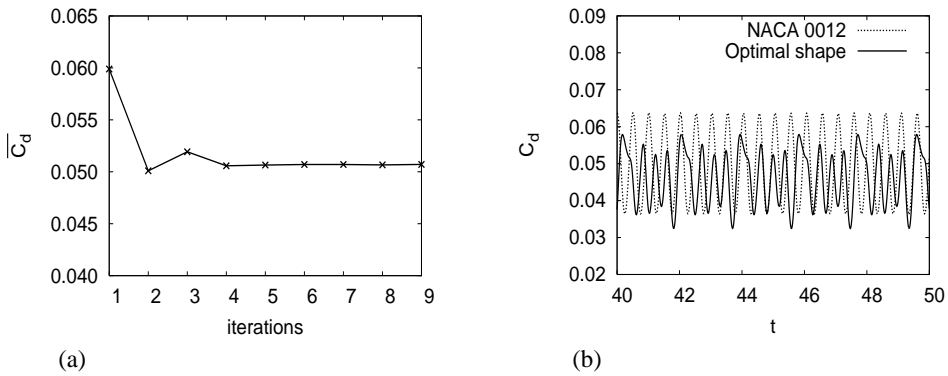


Figure 20: Minimization of $\overline{C_d}$ at $Re = 10^4$ and $\alpha = 5^\circ$: (a) iteration history of $\overline{C_d}$ (b) time history of C_d for initial and optimal shapes.



Figure 21: Minimization of $\overline{C_d}$ at $Re = 10^4$ and $\alpha = 5^\circ$: time-averaged streamlines for (a) NACA 0012 (b) optimal shape.

the optimal airfoil obtained has higher aerodynamic efficiency than the NACA 0012. The time-averaged streamlines for the NACA 0012 and the optimal shape

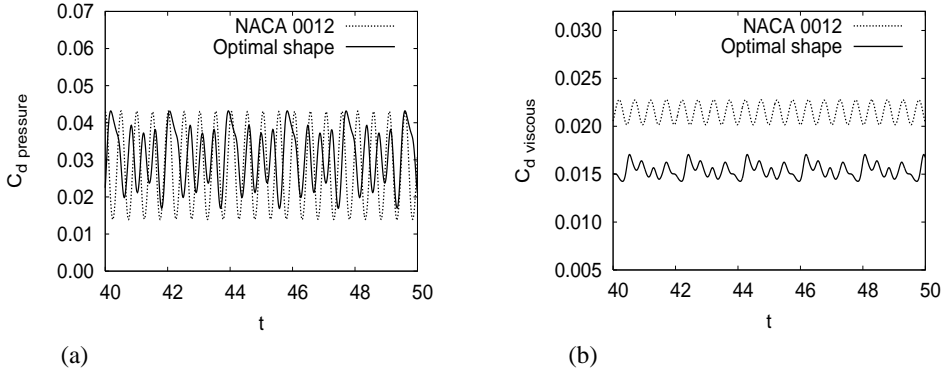


Figure 22: Minimization of $\overline{C_d}$ at $Re = 10^4$ and $\alpha = 5^\circ$: time history of (a) pressure drag for NACA 0012 and optimal shape (b) viscous drag for NACA 0012 and optimal shape.

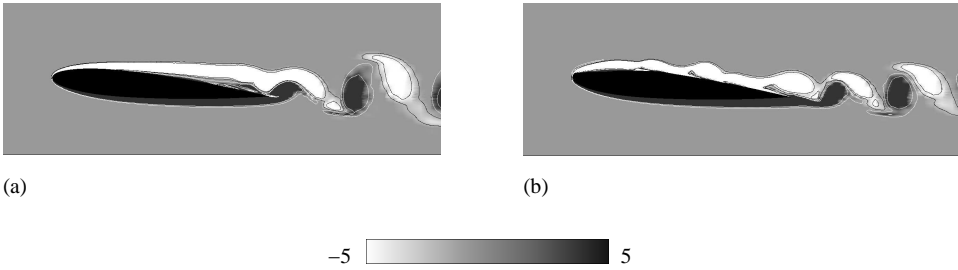


Figure 23: Minimization of $\overline{C_d}$ at $Re = 10^4$ and $\alpha = 5^\circ$: instantaneous vorticity field at $t = 44.5$ for (a) NACA 0012 (b) optimal shape.

are shown in the Figure 26. The instantaneous vorticity field for the NACA 0012 and optimal shape at $t = 25$ are shown in Figure 27.

The optimal shape obtained for $Re = 10^4$ is shown along with the initial shape in Figure 28. The iteration history of $\overline{C_d}/\overline{C_l}$ is shown in Figure 29. For $Re = 10^4$, the time-averaged drag to lift ratio decreases from 0.27 to 0.117; a decrease of 56.67% over the NACA 0012 airfoil. The iteration histories of time-averaged lift and drag coefficient are shown in Figure 29. It is observed that the $\overline{C_l}$ increases from 0.222 to 0.665; an increase of 199.55%, whereas $\overline{C_d}$ increases from 0.060 to 0.078; an increase of 30% over the NACA 0012 airfoil. But the relative increase in $\overline{C_l}$ is higher than that of $\overline{C_d}$, hence the optimal airfoil obtained has higher aerodynamic

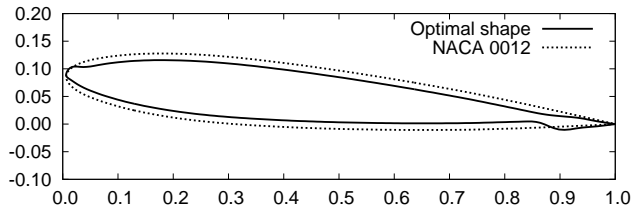
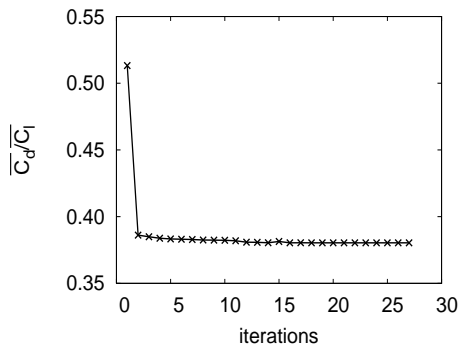
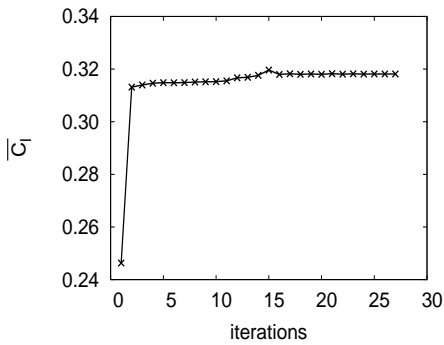


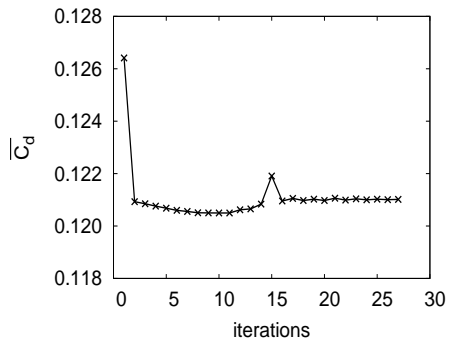
Figure 24: Initial and optimal shapes for minimization of $\overline{C_d}/\overline{C_l}$ at $Re = 10^3$ and $\alpha = 5^\circ$.



(a)



(b)



(c)

Figure 25: Minimization of $\overline{C_d}/\overline{C_l}$ at $Re = 10^3$ and $\alpha = 5^\circ$:(a) iteration history of $\overline{C_d}/\overline{C_l}$ (b) iteration history of $\overline{C_l}$ (c) iteration history of $\overline{C_d}$.

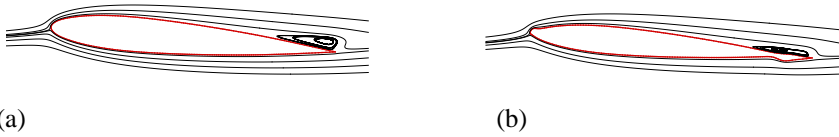


Figure 26: Minimization of $\overline{C_d}/\overline{C_l}$ at $Re = 10^3$ and $\alpha = 5^\circ$: time-averaged streamlines for (a) NACA 0012 (b) optimal shape.

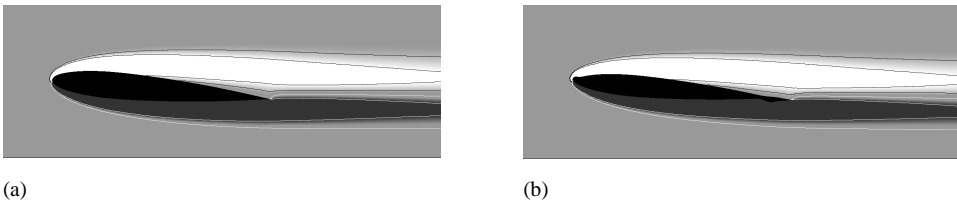


Figure 27: Minimization of $\overline{C_d}/\overline{C_l}$ at $Re = 10^3$ and $\alpha = 5^\circ$: instantaneous vorticity field at $t = 25$ for (a) NACA 0012 (b) optimal shape.

efficiency than NACA 0012. The time-averaged streamlines for the NACA 0012 and the optimal shape is shown in the Figure 30. The instantaneous vorticity field for the NACA 0012 and optimal shape at $t = 45$ are shown in Figure 31.

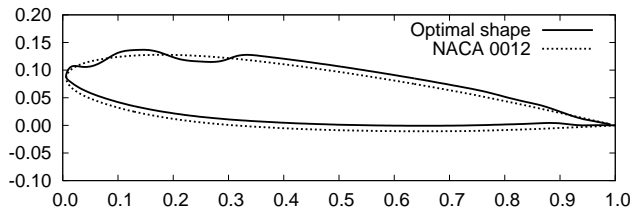


Figure 28: Initial and optimal shapes for minimization of $\overline{C_d}/\overline{C_l}$ at $Re = 10^4$ and $\alpha = 5^\circ$.

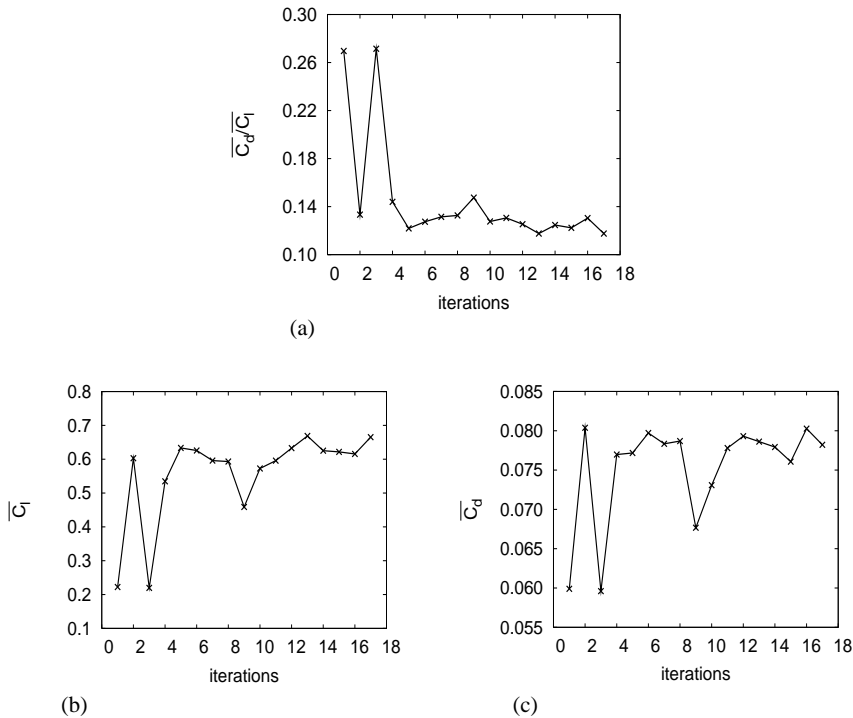


Figure 29: Minimization of $\overline{C_d}/\overline{C_l}$ at $Re = 10^4$ and $\alpha = 5^\circ$: (a) iteration history of $\overline{C_d}/\overline{C_l}$ (b) iteration history of $\overline{C_l}$ (c) iteration history of $\overline{C_d}$.

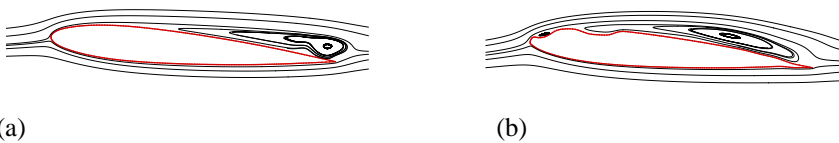


Figure 30: Minimization of $\overline{C_d}/\overline{C_l}$ at $Re = 10^4$ and $\alpha = 5^\circ$: time-averaged streamlines for (a) NACA 0012 (b) optimal shape.

3.4 Effect of time averaging

It is observed from the iteration history of $\overline{C_l}$ shown in Figure 10 that for the case of lift maximization at $Re = 10^4$, $\alpha = 5^\circ$, the convergence of $\overline{C_l}$ is not good. This is due to the fact that the flow obtained for the optimal shape is non periodic. Therefore,

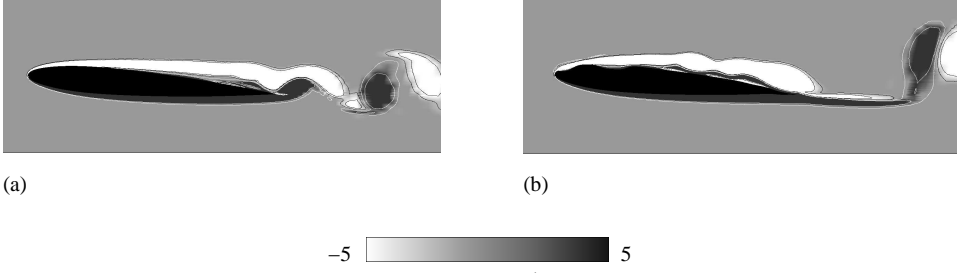


Figure 31: Minimization of $\overline{C_d}/\overline{C_l}$ at $Re = 10^4$ and $\alpha = 5^\circ$: instantaneous vorticity field at $t = 45$ for (a) NACA 0012 (b) optimal shape.

if the flow is not averaged for sufficient time, the value of $\overline{C_l}$ is expected to change from one iteration of the optimization cycle to another, even if the shape does not change much. One way of improving convergence is to average the flow over a longer period of time. The effect of time averaging is investigated for five values of Reynolds numbers: $Re = 10^3$, 3×10^3 , 5×10^3 , 7.5×10^3 and 10^4 at $\alpha = 5^\circ$. The airfoil shape considered is the optimal airfoil computed for maximization of lift at $Re = 10^4$, $\alpha = 5^\circ$. Computations are carried out for each Re for sufficiently long time. The unsteady data so collected is used to compute $\overline{C_l}$:

$$\overline{C_l}(t) = \frac{\int_t^{T_f} C_l(\eta) d\eta}{\int_t^{T_f} d\eta} \quad (27)$$

Here, T_f is the total time for which the unsteady computations have been carried out. It is 400 time units in the present case. The averaging is done backwards in time starting from T_f to ignore the effect of flow development in the initial period of time. The variation of $\overline{C_l}$ with time is shown in Figure 32(a). Let T_{avg} be the minimum number of time units for which the flow should be averaged so that the variation in $\overline{C_l}$ on any further increase in averaging time is less than 1%. Figure 32(b) shows the variation in T_{avg} with Re . It is observed that for $Re = 10^4$, the flow should be averaged for at least 140 time units, approximately, so that the variation in $\overline{C_l}$ is less than 1%. The value of T_{avg} for lower Re is found to be much smaller.

From the above time averaging study, it can be concluded that in order to improve convergence, the flow should be averaged over a longer period of time. In continuation of this study, another computation is carried out for the objective of maximization of $\overline{C_l}$ at $Re = 10^4$ at $\alpha = 5^\circ$. In this study, the flow is averaged for 200 time units, but the adjoint variables are calculated for 22 time units only. This is done because the adjoint variables are found to increase exponentially with time and become large. This leads to round-off errors. Hence erroneous gradients are obtained

if the adjoint variables are calculated over a long period of time. The initial and optimal shapes obtained for this computation are shown in Figure 33. The iteration histories of \overline{C}_l , for the two cases are compared in Figure 34. In the first case the flow is averaged for 30 time units while in the second case, the flow is averaged for 200 time units. It is observed that when the flow is averaged over a longer period of time, the convergence of the optimization cycle is better, but the time-averaged \overline{C}_l is lesser than that obtained with averaging flow for 30 time units.

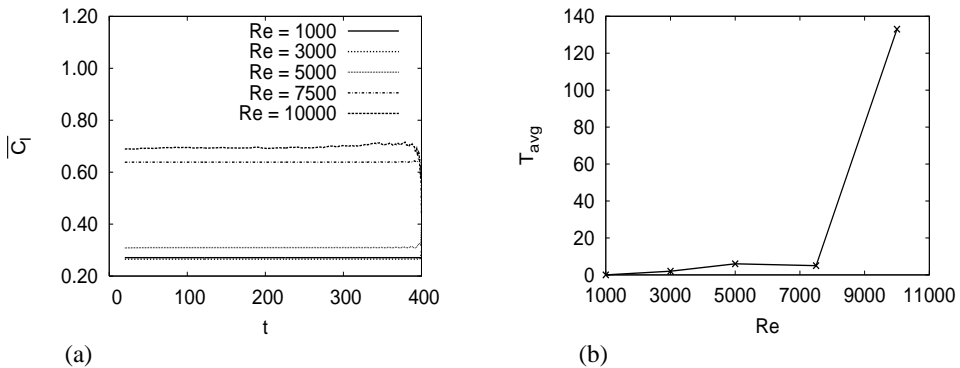


Figure 32: Time averaging study (a) variation of \overline{C}_l with time (b) T_{avg} vs Re . T_{avg} is the minimum time for averaging of flow to keep the error in \overline{C}_l less than 1%.

4 Conclusion

Optimal shape airfoils for different objective functions are obtained by continuous adjoint based optimization method for viscous incompressible unsteady flow at two values of Reynolds numbers: 10^3 and 10^4 , for an angle of attack of 5° . Objective functions used are maximize lift, minimize drag and minimize drag to lift ratio. Interesting shapes are obtained for different objective functions. Table 1 lists the optimal shapes obtained for different objective functions along with the initial shape and their corresponding aerodynamic coefficients at $Re = 10^3$ and $\alpha = 5^\circ$. From Table 1, it is observed that the optimal airfoil obtained for maximization of lift has 36.58% increase in time-averaged lift coefficient than the conventional NACA 0012 airfoil. The optimal airfoil has undulation near the leading edge. Small vortices are formed which sit in the valley of the undulation, hence increasing the suction pressure over the upper surface of the optimal airfoil, therefore increasing the lift. The optimal airfoil obtained for minimization of drag has flatter upper surface compared to NACA 0012. There is 2.1% reduction in time-averaged drag coefficient from the

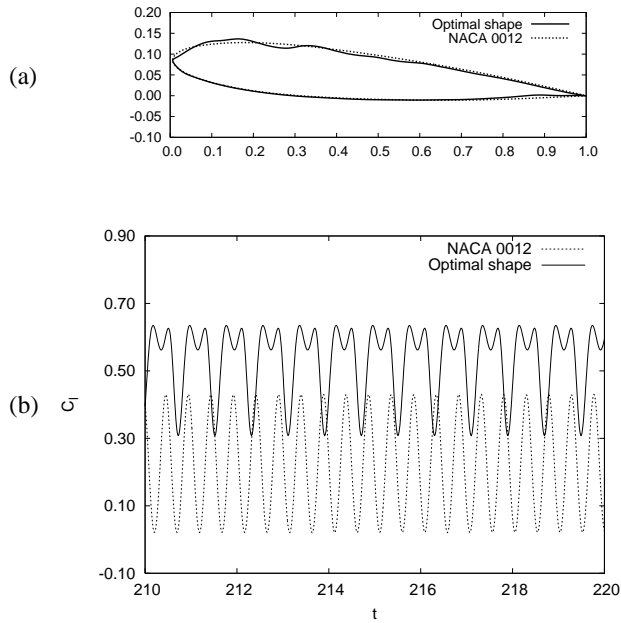


Figure 33: Maximization of \overline{C}_l at $Re = 10^4$ and $\alpha = 5^\circ$ (flow averaged for 200 time units) (a) initial and optimal shapes (b) time history of \overline{C}_l .

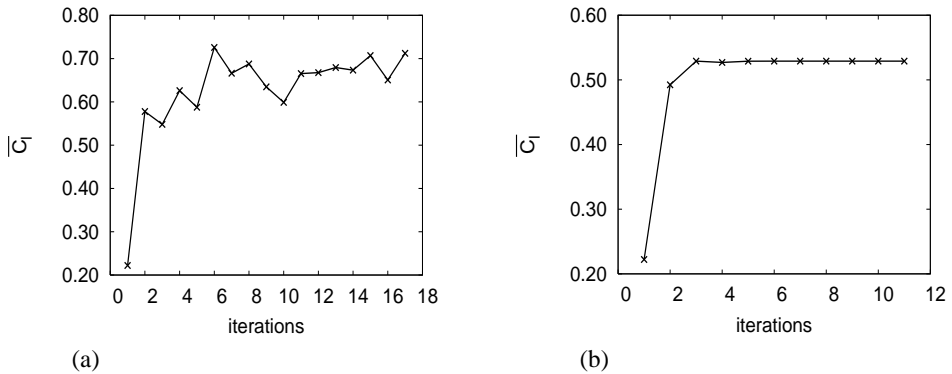


Figure 34: Maximization of \overline{C}_l at $Re = 10^4$ and $\alpha = 5^\circ$: iteration history of \overline{C}_l for flow averaged for (a) 30 time units (b) 200 time units.

NACA 0012 airfoil, which is mainly due to reduction in skin friction. The optimal airfoil obtained for minimization of time-averaged drag to lift ratio looks similar to that obtained for maximization of lift at $Re = 10^3$ and $\alpha = 5^\circ$. The optimal airfoil has 25.53% reduction in drag to lift ratio over the NACA 0012 airfoil.

Table 1: The lift and drag coefficients of the NACA 0012 airfoil and the optimal airfoils at $Re = 10^3$ and $\alpha = 5^\circ$.

I_c	\overline{C}_l	\overline{C}_d	$\overline{C}_l/\overline{C}_d$	Shape
max \overline{C}_l	0.336	0.1260	2.67	
min \overline{C}_d	0.245	0.1238	1.98	
min $\overline{C}_d/\overline{C}_l$	0.318	0.1210	2.63	
NACA 0012	0.246	0.1264	1.95	

Table 2: The lift and drag coefficients of the NACA 0012 airfoil and the optimal airfoils at $Re = 10^4$ and $\alpha = 5^\circ$.

I_c	\overline{C}_l	\overline{C}_d	$\overline{C}_l/\overline{C}_d$	Shape
max \overline{C}_l	0.712	0.0869	8.19	
min \overline{C}_d	0.393	0.0507	7.75	
min $\overline{C}_d/\overline{C}_l$	0.665	0.0782	8.50	
NACA 0012	0.222	0.0599	3.71	

Table 2 lists the optimal shapes obtained for the $Re = 10^4$ flow. The undulations on the upper surface of the optimal airfoil, that are observed for the $Re = 10^3$ flow, are accentuated for the $Re = 10^4$ flow. A 220.72% increase in time-averaged lift coefficient is obtained over the NACA 0012 airfoil. The optimal airfoil obtained

for minimization of time-averaged drag coefficient has flatter upper surface, similar to the optimal airfoil obtained for drag minimization at $Re = 10^3$ and $\alpha = 5^\circ$. Flow separation is delayed in the optimal airfoil and the reduction in drag is mainly due to reduction in skin friction. The optimal airfoil obtained for minimization of drag to lift ratio also has corrugations on the upper surface. The optimal airfoil has 199.55% increase in lift and 30% increase in drag, resulting in 56.67% decrease in drag to lift ratio over the NACA 0012 airfoil.

Effect of time averaging on the convergence of the optimization cycle is studied. It is observed that the flow should be averaged for a sufficient long time to improve the convergence of the optimization cycle.

References

- Anderson, W.; Venkarakrishnan, V.** (1997): Aerodynamic design optimization on unstructured grids with a continuous adjoint formulations. AIAA Paper 97-0643, 1997.
- Bendsoe, M.; Kikuchi, N.** (1988): Generating optimal topology in structural design using a homogenization method. *Computer Methods in Applied Mechanics and Engineering*, vol. 71, pp. 197–224.
- Bendsoe, M.; Sigmund, O.** (1999): Material interpolation schemes in topology optimization. *Archives in applied mechanics*, vol. 69, pp. 635–654.
- Bendsoe, M.; Sigmund, O.** (2002): *Topology Optimization: Theory, Methods and Applications*. Springer-Verlag, Berlin.
- Byrd, R.; Lu, P.; Nocedal, J.; Zhu, C.** (1995): A limited memory algorithm for bound constrained optimization. *SIAM Journal of Scientific Computing*, vol. 16, pp. 1190–1208.
- Cisilino, A.** (2006): Topology optimization of 2D potential problems using boundary elements. *CMES: Computer Modelling in Engineering and Sciences*, vol. 15, pp. 99–106.
- Jameson, A.** (1988): Aerodynamic design via control theory. *Journal of Scientific Computing*, vol. 59, pp. 117–128.
- Juan, Z.; Shuyao, L.; Yuanbo, X.; Guangyao, L.** (2008): A topology optimization design for the continuum structure based on the meshless numerical technique. *CMES: Computer Modelling in Engineering and Sciences*, vol. 34, pp. 137–154.
- Lissaman, P.** (1983): Low-reynolds number airfoils. *Annu. Rev. Fluid Mech.*, vol. 15, pp. 223–239.

- Mueller, T.; DeLaurier, J.** (2003): Aerodynamics of small vehicles. *Annu. Rev. Fluid Mech.*, vol. 35, pp. 89–111.
- Mueller, T.; Kellogg, J.; Ifju, P.; Shkarayev, S.** (2006): Introduction to the design of fixed-wing micro air vehicles. *AIAA Education Series*, vol. 16, pp. 1190–1208.
- Nadarajah, S.; Jameson, A.** (2007): Optimum shape design for unsteady flows with time accurate continuous and discrete adjoint methods. *AIAA Journal*.
- Okamoto, M.; Azuma, A.** (2005): Experimental study on aerodynamic characteristics of unsteady wings at low reynolds number. *AIAA Journal*, vol. 43, pp. 2526–2536.
- Okumura, H.; Kawahara, M.** (2000): Shape optimization of a body located in incompressible Navier-Stokes flow based on optimal control theory. *CMES: Computer Modelling in Engineering and Sciences*, vol. 1, pp. 71–77.
- Spedding, G.; Lissaman, P.** (1998): Technical aspects of microscale flight systems. *J. Avian Biol.*, vol. 29, pp. 458–468.
- Srinath, D.; Mittal, S.** (2007): A stabilized finite element method for shape optimization in low reynolds number flows. *International Journal for Numerical Methods in Fluids*, vol. 54, pp. 1451–1471.
- Srinath, D.; Mittal, S.** (2008): Optimal airfoil shapes for low reynolds number flows. *International Journal for Numerical Methods in Fluids*, vol. 61, pp. 355–381.
- Srinath, D.; Mittal, S.** (2010): An adjoint method for shape optimization in unsteady viscous flows. *Journal of Computational Physics*.
- Srinath, D.; Mittal, S.** (2010): Optimal aerodynamic design of airfoils in unsteady viscous flows. *Computer Methods in Applied Mechanics and Engineering*.
- Srinath, D.; Mittal, S.; Manek, V.** (2009): Multi-point shape optimization of airfoils at low reynolds numbers. *CMES: Computer Modelling in Engineering and Sciences*, vol. 51, pp. 169–190.
- Sunada, S.; Sakaguchi, A.; Kawachi, K.** (1997): Airfoil section characteristics at low reynolds numbers. *J. Fluids Engrg.*, vol. 119, pp. 129–135.
- Tapp, C.; Hansel, W.; Mittelstedt, C.; Becker, W.** (2004): Weight-minimization of sandwich structures by a heuristic topology optimization algorithm. *CMES: Computer Modelling in Engineering and Sciences*, vol. 5, pp. 563–574.
- Vargas, A.; Mittal, R.; ; Dong, H.** (2008): A computational study of the aerodynamic performance of a dragonfly wing section in gliding flight. *Bioinspir. Biomim.*, vol. 3, pp. 26004.

Wang, S.; Lim, K.; Khoo, B.; Wang, M. (2007): A geometric deformation constrained level set method for structural shape and topology optimization. *CMES: Computer Modelling in Engineering and Sciences*, vol. 18, pp. 155–181.

Zhou, M.; Rozvany, G. (2001): On the validity of ESO type methods in topology optimization. *Structural and multidiscipline optimization*, vol. 21, pp. 83–101.

